# Multiparameter Spectrophotometry Platform for Turbid Sample Measurement by Robust Solutions of Radiative Transfer Problems

Peng Tian (田芃) , Yonghong Qin (覃永红) , Lin Zhao (赵林) , Stephen M. Mutisya ,
Jiahong Jin (金佳鸿) , Jun Q. Lu (卢军青) , and Xin-Hua Hu (胡新华)

*Abstract*—Multiparameter spectrophotometer instruments based on the radiative transfer (RT) theory differ fundamentally from conventional ones in their ability to determine absorption and scattering coefficients and anisotropy factor. Ease of use and robustness of inverse solutions are of necessity for general-purpose applications. We have developed a new instrument platform design incorporating a compact three-photodiode detection configuration without integrating spheres, four-channel signal-processing unit, and Monte Carlo (MC) simulation-based software for accurate and rapid inverse solutions. To verify the platform design, two sphere suspension samples of different size distributions were measured and RT parameters were determined by a sample model with the Henyey and Greenstein (HG) phase function between 460 and 1000 nm. System validation is achieved by comparison of the RT parameters and spectral dependence against the results by Mie theory for single-sized spheres of nominal diameter values. Five wavelengths from 560 to 960 nm were selected for quantitative evaluation of the robustness of the HG sample model and two Mie theory-based sample models assuming light scattering by independent and single spheres. We found that only the HG-based sample model yields high accuracy and strong robustness for inverse determination of RT parameters even for the cases of sphere suspensions in which the assumptions of sample uniformity and scattering by independent and single spheres are not satisfied. These results demonstrate that the new platform with MC simulation-based inverse algorithm combined with the HG sample model is capable of robust and rapid measurement of RT parameters for turbid samples with optical thickness up to 30.

*Index Terms*—Light scattering, radiative transfer (RT) theory, spectral measurement, spectrophotometry instrument, turbidity characterization.

Peng Tian and Jiahong Jin are with the Institute for Advanced Optics, Hunan Institute of Science and Technology, Yueyang 414006, China, also with the Department of Physics, East Carolina University, Greenville, NC 27858 USA, also with the Key Laboratory of Hunan Province on Information Photonics and Optical Communication, Hunan Institute of Science and Technology, Yueyang 414006, China, and also with the School of Physics and Electronic Science, Hunan Institute of Science and Technology, Yueyang 414006, China.

Yonghong Qin and Lin Zhao are with the Institute for Advanced Optics, Hunan Institute of Science and Technology, Yueyang 414006, China, and also with the School of Physics and Electronic Science, Hunan Institute of Science and Technology, Yueyang 414006, China.

Stephen M. Mutisya is with the Department of Physics, East Carolina University, Greenville, NC 27858 USA.

Jun Q. Lu and Xin-Hua Hu are with the Department of Physics, East Carolina University, Greenville, NC 27858 USA, and also with the Institute for Advanced Optics, Hunan Institute of Science and Technology, Yueyang 414006, China (e-mail: hux@ecu.edu).

Digital Object Identifier 10.1109/TIM.2020.3032184

## I. INTRODUCTION

SPECTROPHOTOMETRY and infrared spectroscopy often serve as the tools of choice for material analysis by their ease of use to acquire spectral data. The data can be presented in the form of either sample absorbance $A(\lambda) = \log(1/T_c(\lambda))$ or attenuation coefficient $\mu_t(\lambda) = 2.30A(\lambda)/D$, where $\lambda$ is wavelength, $T_c$ the measured signal of collimated transmittance, and $D$ the sample thickness along the direction of incident light beam. Conventional instrument designs for determination of $A(\lambda)$ or $\mu_t(\lambda)$ are founded on the assumption that light attenuation is dominated by atomic and/or molecular absorption [1]–[3]. The assumption, however, breaks down if light scattering is no longer negligible. One must then consider the effect of scattering on measured signals and solve the challenging problems of forward modeling of light scattering and inverse parameter extraction. In return, multiple sample parameters with wavelength dependence enhance markedly the ability to characterize materials by quantification of molecular composition through absorption parameter and wavelength-scaled structures through scattering parameters. Over the past decades, numerous light scattering models of different approximations have been developed and combined with efficient inverse algorithms to retrieve sample parameters from measured signals [4]–[6]. Various spectrophotometric system designs incorporated these methods to determine absorption and scattering parameters in academic laboratory settings. Nearly all designs require integrating spheres for hemispherically integrated measurement of signals and fast parameter extraction from the signals [2], [7]–[13].

We have recently reported a new method for inverse determination of absorption coefficient $\mu_a$, scattering coefficient $\mu_s$, and anisotropy factor g of a turbid sample based on the widely accepted radiative transfer (RT) theory [14]. A three-photodiode configuration was designed to measure diffuse reflectance $R_d$, diffuse transmittance $T_d$, and forward transmittance $T_f$. Without detection of $T_c$ and integrating

spheres for detection of $R_d$ and $T_d$, the new design allows measurement of optically thick samples with significantly reduced burdens of sample preparation and system maintenance. Furthermore, a Monte Carlo (MC) method has been applied to ensure accuracy for calculation of signals arising from light radiance $L(\mathbf{r}, \mathbf{s})$ within the sample, which can be understood by the following steady-state RT equation [4]:

$$\mathbf{s} \cdot \nabla L(\mathbf{r}, \mathbf{s}) = -(\mu_a + \mu_s) L(\mathbf{r}, \mathbf{s}) + \mu_s \int_{4\pi} p(\mathbf{s}, \mathbf{s}') L(\mathbf{r}, \mathbf{s}') d\omega' \tag{1}$$

where $\mathbf{r}$ is a vector of location inside the turbid sample, $\mathbf{s}$ and $\mathbf{s}'$ are unit vectors for incident and scattered directions, and p($\mathbf{s}$, $\mathbf{s}'$) is the single-scattering phase function. An anisotropy factor $g$ can be defined as the mean value of $\cos\theta = \mathbf{s} \cdot \mathbf{s}'$ or the first moment of p($\mathbf{s}$, $\mathbf{s}'$) for quantifying angular distribution of light scattering. Past studies have established that directional distribution of scattered light in term of $g$ presents significant information to distinguish microstructures of materials and tissues for diagnostic purposes [15]–[17]. RT parameters of $\mu_a$, $\mu_s$, and $g$ can be solved inversely as functions of $\lambda$ by comparing iteratively calculated signals, based on (1) and valid boundary conditions, to the measured ones until they become sufficiently close.

Different from $\mu_a$ and $\mu_s$ as scalar parameters, the phase function p($\mathbf{s}$, $\mathbf{s}'$) distributes on unit sphere embedded in $\mathbb{R}^3$ and plays a central role in modeling light scattering. Even by assuming axially symmetric scattering to simplify p($\mathbf{s}$, $\mathbf{s}'$) into p($\cos\theta$), its determination for an unknown sample requires signal measurement at large number of angles. Retrieval of the phase function is obviously impractical for spectroscopic instrumentation. It is thus crucial to identify and validate an effective function for p($\cos\theta$) that allows rapid and robust inverse calculations of RT parameters with only g retrieved for quantifying scattering anisotropy. Various parameterized and light scattering model based functions have been investigated for use as p($\cos\theta$). These include Mie theory-based ones for sphere suspensions, Rayleigh phase function for particles of small size parameters, and various combined parameterized functions [18]–[23]. Among these choices, the function $p_{HG}(\cos\theta)$ proposed by Henyey and Greenstein (HG) stands out as the most commonly used one [24]. The advantages of $p_{HG}(\cos\theta)$ include insensitivity to detailed angular dependence of scattered signals due to a smooth angular dependence, high computing efficiency in numerical simulations by MC methods, and excellent speed for inverse calculations because only $g$ is needed for $p_{HG}(\cos\theta)$. It should be noted that the smooth angular dependence of $p_{HG}(\cos\theta)$ is of little concern since very few turbid materials are of particulate structures with homogeneous and highly symmetric-shaped particles. Many materials have elementary structures like biological cells or other particles in different shapes, structures, and orientations so that their phase functions exhibit smooth angular dependence due to ensemble averaging of different elements [25]–[28]. The major limitation for use of $p_{HG}(\cos\theta)$ as p($\cos\theta$) lies in its monotonic angular dependence for a specific value of g that may differ from angular dependence of certain turbid sample types like biological cells. For example, the HG functions with
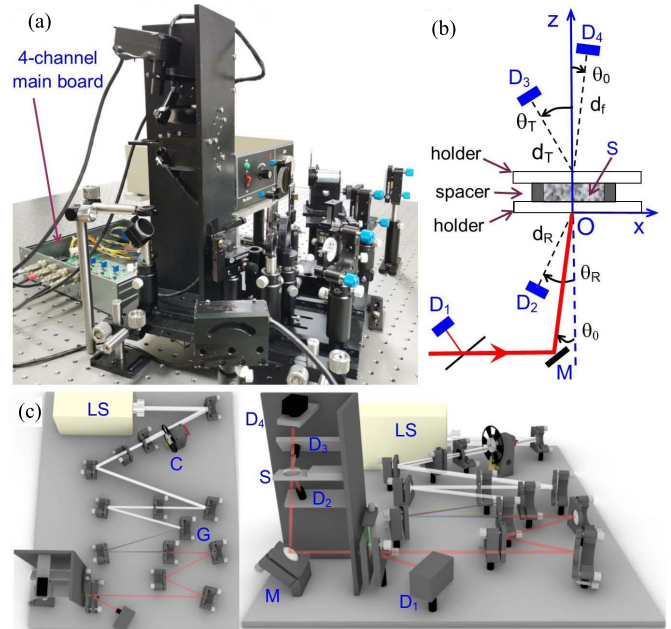


Fig. 1. (a) Photograph of system hardware. (b) Assemblies of sample-holder and three-photodiode detectors: M = mirror, S = sample, $\theta_0$ = incident angle, $\theta_R$ and $d_R$ ($\theta_T$ and $d_T$) = angle and distance of $D_2$ ($D_3$) for measuring $R_d$ ($T_d$), $d_f$ = distance of $D_4$ for measuring $T_f$. (c) Top and side views of system 3-D rendering: LS = light source, C = chopper, and G = grating.

$g > 0$ leads to underestimation of diffusely reflected light intensity for $\theta > 90°$ and particularly for $\theta$ close to $180°$ [29]. Quantitative evaluation of the HG function and related sample model on solving inverse RT problems, however, remains to be investigated, which is especially important for developing robust multiparameter spectrophotometric instruments.

In this article, we present results of a study to develop a prototype system, validate and evaluate a new instrument platform design for multiparameter spectrophotometric measurement based on the RT theory. The prototype employs the three-photodiode detection configuration without integrating spheres and MC simulation-based inverse algorithm for determination of RT parameters. Two sphere suspension samples were prepared for this study and a sample model with the HG function for p($\cos\theta$) was applied for retrieving the RT parameters between 460 and 1000 nm. The system was validated by comparing the above results to those obtained by the Mie theory for single-sized spheres of nominal diameter values. Furthermore, signals measured at five wavelengths were selected to evaluate the robustness of the HG samples models against two other sample models with Mie theory-based phase functions for spheres of different size distributions. By calculating the distribution of an objective function in the parameters space of each sample model, we demonstrate that the HG model exhibits strong robustness for all cases of samples and wavelengths.

## II. HARDWARE DESIGN AND SAMPLE PREPARATION

### A. System Hardware Design and Signal Measurement

A prototype system has been constructed for this study. Its hardware has four units of light source, monochromator,
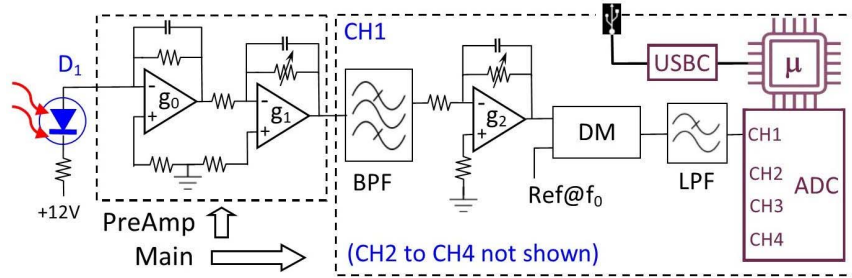
Fig. 2.   Schematics of preamplifier and main board of four-channel lock-in circuit for one channel: $g_0$, $g_1$, $g_2$ = gains of signal amplifiers; BPF = bandpass filter; Ref@ $f_0$ = reference signals of frequency $f_0$ from chopper controller; DM = demodulator; LPF = low-pass filter; ADC = A/D convertor; $\mu$ = microprocessor; USBC = USB controller.

sample chamber, and signal processing boards. Fig. 1 shows a system photograph and layout diagrams of signal detection configuration and beam optics. The light source unit includes an 175-W xenon light source (XL1-175-A, WavMed Technologies Corp., Tianjin, China) of wide emission spectrum from 300 to 2500 nm and beam shaping optics. The mirror-based optical layout implements a Kohler illumination design for control of beam size and intensity separately by two diaphragms. A mechanical chopper (SR540, Stanford Research Systems, Sunnyvale, CA, USA) is used to modulate the output beam at a frequency of $f_0 = 385$ Hz before entering into an in-house built monochromator. The Czerny–Turner design-based monochromator supplies a beam of wavelength $\lambda$ tunable from 460 to 1000 nm and half-maximum bandwidth $\delta\lambda$ of about 4.7 nm by rotating a reflective diffraction grating of 1200 lines/mm (GR1205, Thorlabs, Newton, NJ, USA). The relative large value of $\delta\lambda$ enables an incident beam of adequate intensity with sufficient resolution for our wavelength scanning stepsize $\Delta\lambda$ of 20 nm. The beam is passed through an iris (not shown in Fig. 1) after a turning mirror [M in Fig. 1(b)] to obtain a cylindrical profile on the front surface of assembly with major and minor diameters measured as 10.4 and 4.2 mm, respectively. The half-divergence-angles were found to be 1.3° and 0.21°. A photodiode $D_1$ is employed to monitor the intensity of incident beam $I_0$ as shown in Fig. 1(b).

The sample chamber houses two assemblies of sample-holder and three-photodiode detectors of $D_2$ to $D_4$ (FDS100, Thorlabs) to acquire, respectively, the scattered light intensity signals of $I_{Rd}$, $I_{Td}$, and $I_{Tf}$. Another photodiode $D_1$ is used to monitor incident light intensity $I_0$ and all photodiodes have the same sensor area of $3.6 \times 3.6$ (mm$^2$). The photodiode outputs are measured at each scanned wavelength to determine three measured signals of diffused reflectance $R_d = I_{Rd}/I_0$, diffused transmittance $T_d = I_{Td}/I_0$, and forward transmittance $T_f = I_{Tf}/I_0$. These detectors are installed at the end of black plastic shielding tubes so that their field-of-views are limited to the front or back surface of the sample to prevent receiving light scattered from nonblack surfaces inside the chamber. Detector $D_4$ is placed along the collimated transmission direction at a larger and adjustable distance $d_f$ ranging from 50 to 90 mm so that $T_f$ could be kept on the same scale as $R_d$ and $T_d$, which improves convergence of inverse calculations by the HG sample model. The solid angles for acquisition of the $R_d$ and $T_d$ signals are kept in a range of 0.01–0.03 sr to yield sufficient angular integration over the detector sensor surface based on

our earlier experimental results [12]. The detector distances of $D_2$ to $D_4$ can be adjusted from the sample assembly for different samples to increase signal-to-noise ration and avoid detector saturation. The same configurations of sample and detector assemblies are implemented in our MC simulations to accurately determine calculated signals as discussed later.

The signal-processing unit includes four preamplifiers placed close to respective photodiodes and a four-channel lock-in main board connected to a host computer. Fig. 2 presents the schematics of the boards. Each current signal from a negatively biased photodiode is converted into a voltage signal followed by amplification of gain $g_1$ before output from the preamplifier board. The signal is further bandpass filtered, amplified with gain $g_2$, demodulated by a balanced modulator (AD630, Analog Devices, Norwood, MA, USA), and low-pass filtered before digitization by a 24-bit A/D convertor (AD7739, Analog Devices) in the main board. The convertor's output is read by a microprocessor (ATMega32U4, Atmel, San Jose, CA, USA), which handles command and data communications with the host computer via an USB cable and controls amplifier gains of $g_1$ and $g_2$ by digital potentiometers.

*B. Sample Preparation and Characterization*

We chose sphere suspensions as samples for the validation of the platform design and evaluation of the performance of three samples models in inverse determination of RT parameters. Two samples were prepared by diluting purchased polystyrene sphere suspensions with deionized water. The nominal diameters and coefficients of variation (CV) are provided by vendors as $d_s = 0.966$ $\mu$m and CV = 1.3% (5095B, Duke Scientific, Fremont, CA, USA) for sample A and $d_s = 11$ $\mu$m and CV $\leq 18\%$ (7510B, ThermoFisher Scientific, Waltham, MA, USA) for sample B. Sphere concentrations $\rho_s$ were determined by the masses of suspension and dry sphere component and found to be $(5.37 \pm 0.02) \times 10^6$ mm$^{-3}$ for sample A and $(3.05 \pm 0.02) \times 10^4$ mm$^{-3}$ for sample B using an evaporation method [30]. The front and back slabs of the sample holder were cut from microscope glass slides with thickness around 1.0 mm. The sphere suspension was confined by a ring spacer of 14.3 mm in diameter between the two glass slabs. The sphere size distributions were imaged by a microscope using an objective of $40\times$ and 0.65 in NA. The areas of single spheres were measured by a software to determine their diameters and Gaussian curve fitting was applied
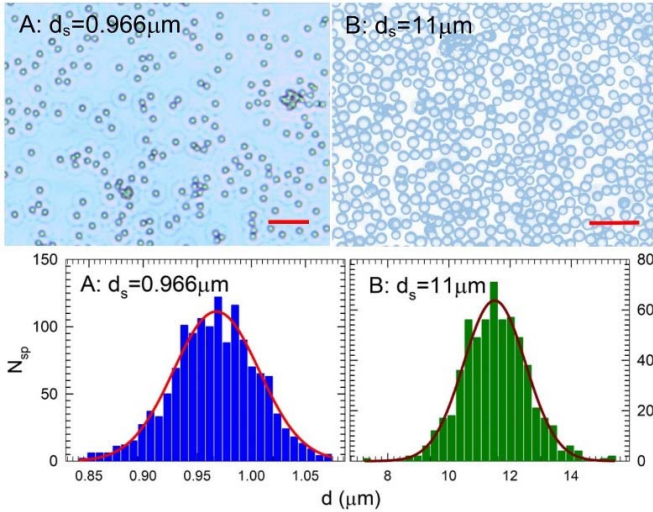
Fig. 3. Images of the sphere suspension sample A with bar = 10 $\mu$m and sample B with bar = 50 $\mu$m (top row). Histograms with $N_{sp}$ as number of spheres, $d$ as measured diameter values and Gaussian distributions curves by solid lines (bottom row).

to the histogram of measured diameter data. Fig. 3 presents the microscopy images and histograms of size distributions. We determined the mean value and standard deviation of sphere diameters for the sample A as $\mu'_d = 1.80$ $\mu$m and $\sigma'_d = 0.073$ $\mu$m. The value of $\mu_d$ was much larger than $d_s$ by a factor of 1.86 that can be attributed to the relative low accuracy in area calculations due to edges blurred by the interference rings. To correct the area measurement errors, the histogram data in Fig. 3 for sample A were scaled by the factor of 1.86 for diameter values so that the scaled values were given by $\mu_d = d_s$ and $\sigma_d = 0.040$ $\mu$m. The sphere parameter for sample B was found to be $\mu_d = 11.5$ $\mu$m and $\sigma_d = 1.0$ $\mu$m by the Gaussian curve fitting with no scaling.

## III. SYSTEM SOFTWARE DESIGN

The software of prototype system has three components for data acquisition, light scattering simulation, and inverse calculations with Fig. 4 showing flow charts of the first two. Data acquisition was controlled through the microprocessor which synchronizes the wavelength tuning, signal digitization, determination, and export of the measured signals. Simulation of light scattering yields calculated signals from a chosen sample model and RT parameters as input data. The red-lined block in Fig. 4(b) presents the core of light scattering modeling which is the focus of this study for system validation and performance evaluation.

### A. Signal Calculation by iMC Simulation

An individual photon tracking MC (iMC) code has been developed to calculate signals with the detector configuration illustrated in Fig. 1(b). Details of the code, validation results, and GPU implementation have been published elsewhere and are briefly described below [9], [17], [31]–[33]. At each wavelength, initial or iterated values of RT parameters are imported into the iMC code together with a selected function for p(cos$\theta$) according to the selected sample model. An incident light

beam is represented in iMC by $N_0$ photons on the front surface of sample holder with an incident angle of $\theta_0$. A total length $L_a$ is determined from $\mu_a$ and a random number (RN) uniformly distributed in (0,1) for each tracked photon before it enters the sample assembly. Then each photon propagates through or becomes reflected off various index mismatched interfaces among air, holder glass slab, and sample according to the local Fresnel reflectance. Once a photon moves into the turbid sample, its trajectory evolves as a sequence of segments of pathlengths $L_{sj}$ ($j = 1, 2, \ldots$) determined by $\mu_s$ and updated scattering angle $\theta$ by the selected phase function and RNs. At the end of $L_{sj}$, the accumulated pathlength $L_s = \sum_{j'=1}^{j} L_{sj'}$ is compared to $L_a$. If $L_s > L_a$, the photon is terminated as being absorbed; otherwise it is propagated further until reaching a sample surface. When the photon exits a sample holder glass into air, the code further checks if it hits a detector and increments the related photon counter for affirmative answer. Finally, the calculated signals of $R_{dc}$, $T_{dc}$ and $T_{fc}$ are obtained by dividing the number of photons reaching a respective detector by $N_0$.

For iMC simulations with a selected phase function based on the Mie theory in numerical form only, a lookup table of 5000 elements is compiled and used as input data of iMC for determination of scattering angles. At each scattering site for a tracked photon inside the sample, the following inequalities are evaluated using the lookup table and an RN [34]:

$$2\pi \sum_{k=1}^{K-1} p(x_k)\Delta x_k \leq \text{RN} \leq 2\pi \sum_{k=1}^{K} p(x_k)\Delta x_k \qquad (2)$$

to derive a proper value of $x_K$ and the scattering polar angle $\theta = \cos^{-1} x_K$. The scattering azimuthal angle $\varphi$ is set to an RN uniformly distributed on $[0, 2\pi]$ for all sample models. The iMC code has been validated against the bidirectional curves of reflection $R_b$ and transmission $T_b$ of turbid samples of an infinite slab with different combinations of RT parameters compiled in [4].

### B. Solving Inverse RT Problems

An objective function $\delta$ is defined as the squared error between the measured and calculated signals that is given by

$$\delta = \left(\frac{R_d - R_{dc}}{R_d}\right)^2 + \left(\frac{T_d - T_{dc}}{T_d}\right)^2 + \left(\frac{T_f - T_{fc}}{T_f}\right)^2. \qquad (3)$$

Inverse determination of the RT parameters $\mu_a$, $\mu_s$, and $g$ from the measured signals at $\lambda$ is framed as solving an optimization problem toward $\delta \leq \delta_0$ through iteration. For this report, we set the value of $\delta_0$ at $8 \times 10^{-3}$ which corresponds to about $\pm 5\%$ for averaged relative errors in the measured signals of $R_d$, $T_d$, and $T_f$ for the prototype system. A gradient descent-based algorithm was applied to update RT parameters for iMC simulations and to make $R_{dc}$, $T_{dc}$, and $T_{fc}$ approach to the measured signals with $\delta \leq \delta_0$ [17].

To speed up inverse calculations, iMC simulations have been implemented for parallel execution on a GPU board (Tesla K20, Nvidia, Santa Clara, CA, USA). The current iMC-GPU code has a speedup of about 70 relative to execution on a CPU of 2.93 GHz (i7-870, Intel, Santa Clara, CA, USA).
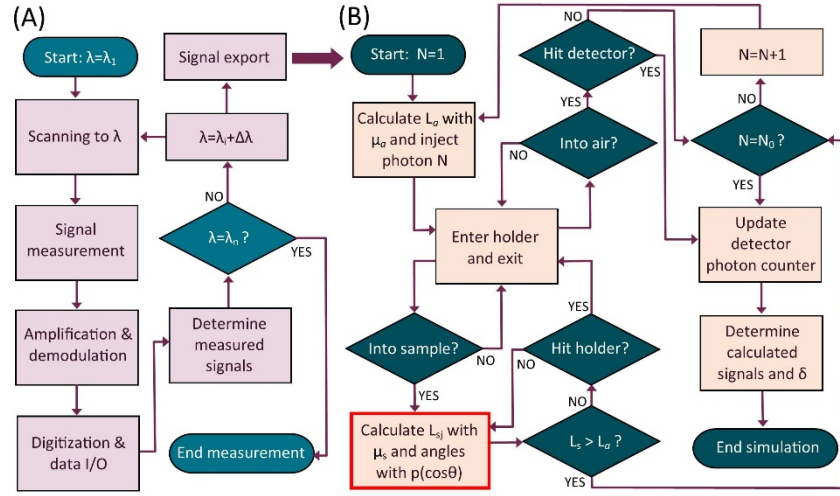
Fig. 4. Flowcharts of software components. (A) Acquisition of measured signals over scanned wavelengths of stepsize $\Delta\lambda$. (B) iMC simulation of calculated signals with $N_0$ incident photons at a scanned wavelength.

Simulation time depends mainly on the values of $\mu_a$ and $\mu_s$ for a given sample size and total photon number $N_0$. It took 5.2 s to complete an iMC-GPU simulation with $\mu_a = 0.29$ mm$^{-1}$, $\mu_s = 4.74$ mm$^{-1}$, and $N_0 = 5 \times 10^7$ for sample A with averaged statistical fluctuations in calculated signals at about 1.4%. Since much larger fluctuations can be tolerated in the initial search for $\delta$ far from $\delta_0$ in parameter space, the value of $N_0$ for iMC simulations was set to $5 \times 10^6$ for initial search and increased to $5 \times 10^7$ as $\delta$ moves toward $\delta_0$. Thus, it took about 10 min or less on average to determine RT parameters at the first wavelength of a sample with mean numbers of iterations around 400. The time of inverse solution per wavelength was further decreased to about 5 min or less as a result of closer initial parameter values from the results of last wavelength and smaller $\mu_s$ values for longer wavelengths.

### C. Modeling of Sphere Sample With Different Phase Functions

For quantitative evaluation of the HG sample model, we constructed two additional sample models by the Mie theory that solves the vector wave equations of light scattering by a homogeneous sphere with a closed-formed solution. Different from the HG model with three adjustable parameters of $\mu_a$, $\mu_s$, and $g$, the two Mie-based models have dissimilar size distributions and number of adjustable parameters. One is for single-sized homogeneous polystyrene spheres in water with $p_{MS}(\cos\theta, d)$ as the phase function and $d$ as the only adjustable parameter of sphere diameter. The other is for multisized spheres with $p_{MM}(\cos\theta)$ as the phase function and two adjustable parameters of $\mu_d$ as the mean value and $\sigma_d$ as standard deviation of diameters. The two sample models are denoted, respectively, as the Mie-single-sized (MS) and Mie-multisized (MM) models.

A Mie code was utilized to develop a code for calculation of the $4 \times 4$ Mueller matrix $[S_{ij}(\cos\theta, d): i, j = 1, \ldots, 4]$ as intensities of polarized light scattered by a sphere of diameter $d$ [35]. Other input parameters include the complex refractive index (RI) of sphere $n_s$, real RI of host medium $n_h$ by water

and $\lambda$ [30], [36]. The element $S_{11}$ in the output data provides the differential scattering cross section to unpolarized incident light which was normalized as the scattering phase function $p_{MS}(\cos\theta, d)$ for the MS sample model of single-sized spheres. For the MM model of multisized spheres, we employed a Gaussian distribution function $G(d)$ based on the histogram data in Fig. 3 to obtain a phase function given by [20]

$$p_{MM}(\cos\theta) = \int_0^\infty G(d) p_{MS}(\cos\theta, d) d(d)$$
$$\approx \sum_{q=1}^Q G(d_q) p_{MS}(\cos\theta, d_q) \qquad (4)$$

where

$$G(d) = \frac{1}{\sigma_d \sqrt{2\pi}} e^{-\left(\frac{d-\mu_d}{\sqrt{2}\sigma_d}\right)^2}. \qquad (5)$$

We set $Q = 25$ for numerical calculation of $p_{MM}(\cos\theta)$ for this study. The RT parameters of $\mu_a$, $\mu_s$, and $g$ were obtained from the size distributions, and the total cross sections of absorption $\sigma_a(d_q)$ and scattering $\sigma_s(d_q)$ are as follows:

$$\mu_a = \sum_{q=1}^Q \rho(d_q)\sigma_a(d_q) = \rho_s \sum_{q=1}^Q G(d_q)\sigma_a(d_q)$$

$$\mu_s = \sum_{q=1}^Q \rho(d_q)\sigma_s(d_q) = \rho_s \sum_{q=1}^Q G(d_q)\sigma_s(d_q)$$

$$g = 2\pi \int_{-1}^1 x p_{MM}(x) dx \qquad (6)$$

where $\rho(d_q) = \rho_s G(d_q)$ is the number density of single spheres with diameter $d_q$ and $\rho_s$ as the measured number density of spheres in each sample. For the MS model, the sums in (6) for $\mu_a$ and $\mu_s$ were reduced to a single term of diameter $d$ and $g$ directly from the Mie code.

### IV. SYSTEM VALIDATION AND MODEL EVALUATION

#### A. Platform Validation

Measurements of nonhemispherical signals of $R_d$, $T_d$, and $T_f$ were repeated three times at each wavelength from 460 to
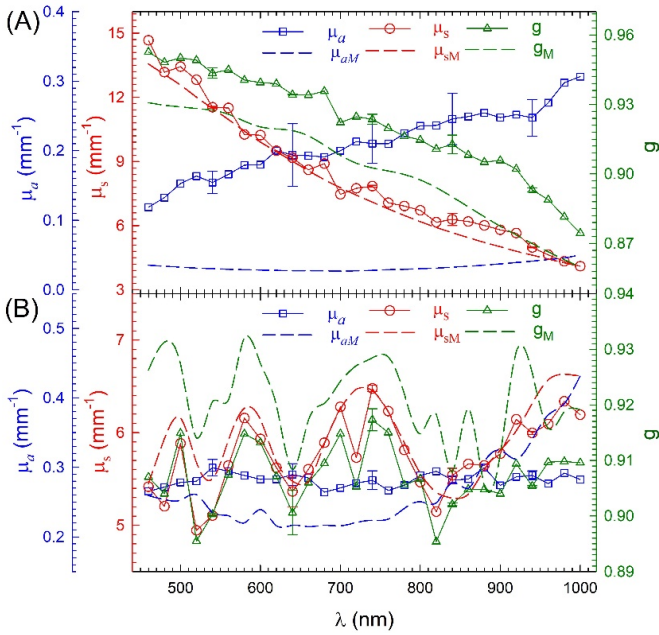
Fig. 5. Wavelength dependence of RT parameters. The symbols and error bars are the mean values and standard deviations determined from three sets of measured signals by the HG sample model that are connected by solid lines. (A) Sample A with $d_s = 0.966$ $\mu$m, $\rho_s = (5.37 \pm 0.02) \times 10^6$ mm$^{-3}$, $D = 2.06 \pm 0.01$ mm, $\theta_R = 45°$, $d_R = 31.7$ mm, $\theta_T = 43°$, $d_T = 44.1$ mm, and $d_f = 49.3$ mm. (B) Sample B with $d_s = 11$ $\mu$m, $\rho_s = (3.05 \pm 0.02) \times 10^4$ mm$^{-3}$, $D = 2.10 \pm 0.01$ mm; $\theta_R = 45°$, $d_R = 21.5$ mm, $\theta_T = 48°$, $d_T = 35.7$ mm, $d_f = 88.4$ mm. The distance parameters are defined in Fig. 1(b). The dash lines are RT parameters of sphere suspensions calculated by (6) using the Mie phase function for single-sized spheres with $d_s$ as diameter and $\rho_s$ as concentration.

1000 nm with a stepsize of 20 nm by the three-photodiode configuration as shown in Fig. 1 for the two sphere samples. Experimental parameters of incident beam profile, sizes and distances of sample, holder, and detectors were imported into the iMC code to maximize accuracy of calculated signals. RT parameters were determined at each wavelength by iterating iMC simulations for calculated signals by the HG sample model when $\delta \leq \delta_0$ was reached. To validate the platform design, we also applied the Mie theory to obtain the RT parameters of $\mu_{aM}$, $\mu_{sM}$, and $g_M$ in the same wavelength range according to (6) for the two samples assumed as suspensions of single-sized spheres, where the measured value of sphere concentrations $\rho_s$ and the nominal sphere diameter $d_s$ supplied by vendors were used. The two sets of RT parameters versus wavelength have been previously reported in [14, Fig. 2] and are replotted in Fig. 5 for completeness of discussion.

Among the three RT parameters shown in Fig. 5, the values and $\lambda$ dependence of $\mu_s$ agree quite well with those of $\mu_{sM}$ for the two samples of $\mu_s \gg \mu_a$, with better agreement for sample A exhibiting a monotonic dependence. In comparison, the agreements between the absorption coefficients of $\mu_a$ and $\mu_{aM}$ deteriorate significantly. A closer look of the $\mu_a$ differences suggests that the current platform design using the three-photodiode detection configuration is likely to have a lower limit in $\mu_a$ determination that likely is around 0.2 mm$^{-1}$. This conclusion is corroborated by the case of sample B in which the differences reduce considerably for $\mu_a$ values

staying above 0.2 mm$^{-1}$. For anisotropy factor g, the $\lambda$ dependence agrees well while the values do not. Since the relative differences of g values are opposite in the two samples, it is unlikely that the disagreement is due to underestimate of light scattering for $\theta > 90°$ by the HG model. Rather, the disagreement of both $\mu_s$ and g between the HG model and Mie theory could be attributed to sphere settling leading to the failure of Mie theory that assumes uniform suspension and independent single spheres. Sphere settling became especially severe for the sample B of larger volume-to-surface ratios with a settling time less than 5 min and the sample had to be shaken before next wavelength of measurement.

Based on the above observations, one may reach the conclusion that the new platform design can accurately determine scattering coefficient $\mu_s$ for homogeneous turbid samples but has a detection floor for absorption coefficient $\mu_a$ at about 0.2 mm$^{-1}$. Without $T_c$ measurement, it is further interesting to observe that optically thick samples can be characterized for optical thickness of $\mu_t D$ up to 30. Inversely determined g values may deviate slightly from "true" values but its wavelength dependence is likely to be accurate for the characterization of scattering anisotropy. In the cases of sample A and B with forwardly peaked scattering patterns, the averaged deviations of g from the Mie predicted values are less than 3%. It should be noted that no adjustable parameters were used in calculation of RT parameters by the Mie theory shown in Fig. 5.

### B. Comparison of Measured and Calculated Signals

From the data displayed in Fig. 5, one cannot find out if the Mie phase functions and RT parameters determined by (6) can yield inverse solutions defined by $\delta \leq \delta_0$. For this purpose, we have applied the two Mie-based sample models in iMC simulations to obtain calculated signals on selected wavelengths for quantitative evaluation of their robustness against the HG sample model. Table I lists the mean values and standard deviations of the measured signals together with configuration parameters of the sample and detector assemblies at five wavelengths. The relative errors of the measured signals range from 0.5% to 8.0% with the averaged value at 2.7%. Because of the strongly peaked scattering in the forward direction of both samples, the measured $R_d$ signal is smaller than those of $T_d$ and $T_f$ if the detectors were placed at similar distances from the sample, which led to larger errors for $R_d$ values of the sample A. The design of prototype system was modified to enable adjustment of detector distances for increasing signal intensity and improve significantly the repeatability of the measured data.

The iMC code was used to obtain the calculated signals of $R_{dc}$, $T_{dc}$, and $T_{fc}$ for each sample model with the given phase function and trial values of RT parameters. With the measured signals, we have investigated the distribution of objective function $\delta$ in the parameter space for robustness evaluation. The parameter space is defined by $\mu_a$, $\mu_s$, and g for the HG model while the corresponding ones are defined by $\mu_d$ and $\sigma_d$ for the MM model and d for the MS model. We determined the objective function $\delta$ with fixed step sizes in the respective parameter space around the locations of minimal

TABLE I

MEASURED DATA OF TWO SPHERE SAMPLES AT FIVE WAVELENGTHS[a]

| $\lambda$ (nm) | Sample A ($d_s$=0.966μm) | | | Sample B ($d_s$=11μm) | | |
|---|---|---|---|---|---|---|
| | $R_d \times 10^4$ | $T_d \times 10^4$ | $T_f \times 10^4$ | $R_d \times 10^4$ | $T_d \times 10^4$ | $T_f \times 10^4$ |
| 560 | 3.87±0.18 | 3.87±0.13 | 4.79±0.074 | 4.46±0.063 | 3.98±0.027 | 1.47±0.016 |
| 660 | 3.37±0.11 | 3.78±0.12 | 4.86±0.028 | 4.64±0.027 | 4.03±0.060 | 1.44±0.036 |
| 760 | 2.99±0.10 | 3.63±0.14 | 4.58±0.071 | 4.84±0.14 | 4.14±0.073 | 1.40±0.064 |
| 860 | 2.67±0.080 | 3.48±0.062 | 4.36±0.022 | 4.79±0.057 | 3.99±0.099 | 1.33±0.094 |
| 960 | 2.37±0.19 | 3.39±0.22 | 4.84±0.052 | 5.05±0.12 | 4.05±0.068 | 1.26±0.064 |

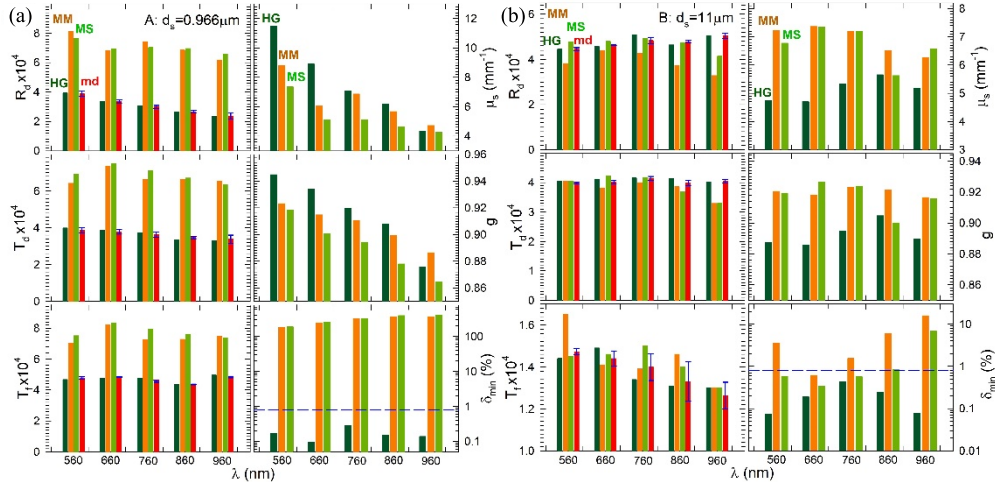[a]The mean values and standard deviations of measured data were obtained by 3 measurements.



Fig. 6. Wavelength dependence of calculated signals against the mean values and error bars of measured data (md), scattering RT parameters of $\mu_s$ and $g$ and $\delta_{min}$ by the HG, MM, and MS models for (a) sample A of $d_s = 0.966$ $\mu$m and (b) sample B of $d_s = 11$ $\mu$m. The blue dash lines represent $\delta_0$ used as the threshold for inverse solutions.

value $\delta_{min}$ and examined if $\delta_{min} \leq \delta_0$ to satisfy the definition of an inverse solution. For the MM and MS sample models, the parameter ranges were set to between 0.6 and 1.2 $\mu$m for $\mu_d$ (or $d$) and between 0.006 and 0.3 $\mu$m for $\sigma_d$ of the sample A based on results of sphere size measurement. For the sample B, the respective ranges were given by between 9.0 and 14 $\mu$m and between 0.8 and 2.5 $\mu$m. The RT parameters were calculated for the MM and MS models by (6) after the sphere size parameters were determined at $\delta_{min}$ for comparison to those of the HG model.

Fig. 6 compares the calculated signals against the measured data by the left-side bar diagrams of (a) and (b) for sample A and B at five wavelengths. The right-side diagrams show the scattering RT parameters of $\mu_s$ and $g$ determined at $\delta_{min}$ among the sample models. These data show clearly that the HG model can yield calculated signals well matched to the measured ones in all cases with the adjustable parameters of $\mu_a$, $\mu_s$, and $g$. The other two models, however, yield inverse solutions with $\delta_{min} \leq \delta_0$ satisfied only in certain cases in the space of $\mu_d$ and $\sigma_d$ or $d$. For sample A, the values of $\mu_s$ and $g$ and their $\lambda$ dependence exhibit fairly good agreement among the three models despite the fact of $\delta_{min}$ being significantly larger than $\delta_0$ for the MM and MS models. For sample B, the Mie-based models improve markedly with $\delta_{min}$ less than or close to $\delta_0$ except the case of $\lambda = 960$ nm. It is in this case,
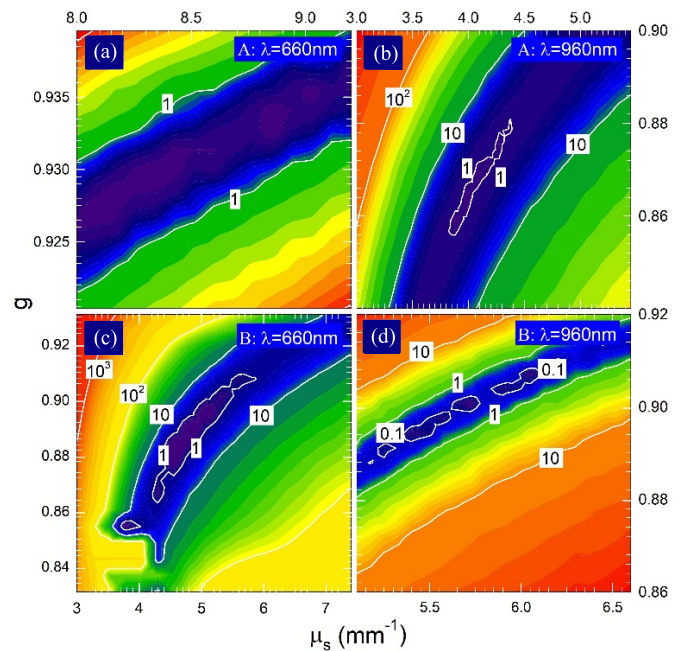


Fig. 7. Contour plots of $\delta$ values in % in the $\mu_s$–$g$ plane of parameter space for the HG model with sample ID and $\lambda$ values as marked for different $\mu_a$ values. (a) $\mu_a = 0.193$ mm$^{-1}$. (b) $\mu_a = 0.269$ mm$^{-1}$. (c) $\mu_a = 0.285$ mm$^{-1}$. (d) $\mu_a = 0.277$ mm$^{-1}$. All iMC simulations were performed with $N_0 = 1 \times 10^8$.

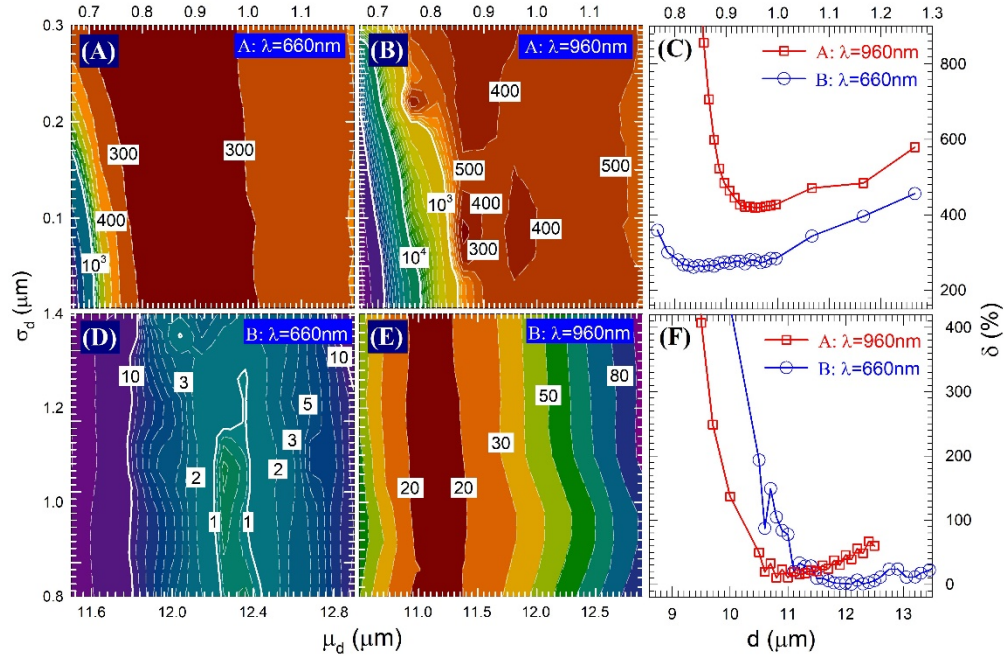Fig. 8. Contour plots of $\delta$ values in % with sample ID and $\lambda$ values marked for different Mie-based sample models. (A) MM. (B) MM. (C) MS. (D) MM. (E) MM. (F) MS. All iMC simulations were performed with $N_0 = 1 \times 10^8$.

very interestingly, that the two Mie-based models can match $T_{fc}$ to $T_f$ with $\mu_s$ and $g$ larger than those of the HG model but yield $R_{dc}$ and $T_{dc}$ significantly smaller than the measured data. This can be explained by the fact that either $p_{MS}(\cos\theta, d)$ or $p_{MM}(\cos\theta)$ for spheres of $d \sim 11 \ \mu$m is of a very high peak value for forward scattering of $\theta \sim 0$ in comparison to $p_{HG}(\cos\theta)$ and smaller values in side scatter of $R_{dc}$ and $T_{dc}$ (see [14, Fig. 3]). It is also worth noting that the measured values of sphere density $\rho_s$ for both samples can produce RT parameters for the Mie-based models in the same ranges of those used for searching inverse solutions by the HG model through (6).

### C. Evaluation of Robustness by $\delta$ Distributions

To better understand the influence of sample model on solving inverse RT problems, we have obtained the maps of $\delta$ functions in the parameter spaces of the three sample models in two cases of $\lambda = 660$ and 960 nm for the two samples. Fig. 7 presents the contour plots of $\delta$ as functions of $\mu_s$ and $g$ with $\mu_a$ kept at the constant value for $\delta = \delta_{\min}$ by the HG model in the four cases of different samples and wavelengths. We note that the numbers of detected photons for the calculated signals fluctuate as a result of statistical variance in iMC simulations. Even with $N_0$ increased to $1 \times 10^8$, these variances can still reach to 1% for calculated signals because the number of detected photons are about $10^4$. This leads to fluctuation of $\delta$ around 0.1% when the measured and calculated signals are very close to each other or $\delta$ becomes close to or less than $\delta_0$. Consequently, multiple local minima are visible, as shown in Fig. 7(a) and (d), by the contour plot software interpolating the fluctuating values of $\delta < 1\%$ in these regions of $\mu_s$ and $g$. Despite these artifacts, the results in Fig. 7 clearly demonstrate that the RT problems defined

by the HG sample model form convex optimization problems. Thus, a global minimum exists that enables inverse solutions by a gradient descent-based algorithm for all cases using $p_{HG}(\cos\theta)$ as the phase function.

Compared to the HG model, the two Mie based models vary significantly in the stability and feasibility for inverse solutions among the different cases of samples and wavelengths. The plots presented in Fig. 8(A)–(C) shows clearly that neither of the MM and MS model can produce calculated signals close to the measured data for sample A satisfying $\delta_{\min} \leq \delta_0$. Furthermore, the values of sphere parameters determined at $\delta_{\min}$ were found to be $\mu_d = 0.76 \ \mu$m and $\sigma_d = 0.30 \ \mu$m by the MM model and $d = 0.84 \ \mu$m by the MS model. These values deviate considerably from the measured values before or after scaling as shown in Fig. 3. For sample B, both Mie-based models can produce calculated signals much closer to the measured data with $\delta_{\min} \leq \delta_0$ as illustrated in Fig. 8(D) and (F) for $\lambda = 660$ nm. Still the sphere diameter values of $\mu_d$ and $d$ are significantly larger than $d_s$ or $\mu_d$ determined by microscopy. For the case of $\lambda = 960$ nm, both models failed to yield inverse solutions even though the d values for $\delta = \delta_{\min}$ are fairly close to $d_s$ for both samples.

The results presented from Figs. 6–8 demonstrate clearly that iMC simulations combined with the HG sample model provide a robust approach for inverse solutions of RT parameters from the measured signals of $R_d$, $T_d$, and $T_f$. In contrast, the Mie theory solves rigorously a light-scattering problem only for uniform sphere suspension samples under the assumption of independent and single spheres. The assumptions of suspension uniformity and independent single spheres, however, can be very difficult to be realized in samples, which should cause the inability of MM or MS model to match calculated signals to measured signals in most cases. Additionally, the sphere concentration $\rho_s$ of sample A was set

high to have sufficient signal-to-noise ratios for the $R_d$ and $T_d$ signals measured by photodiodes. The sample A appears like milk for the high $\rho_s$ value and presented clearly a problem in which the electromagnetic fields scattered by other spheres must be considered together with those of the incident light for the considered sphere. Therefore, the failure of MM and MS models to yield inverse solutions defined by $\delta < \delta_0$ for sample A can be attributed to violation of the assumptions for sample uniformity and independent single spheres. Based on these considerations, the improvement of the Mie-based models in the case of sample B can be regarded as a consequence of decreased $\rho_s$ as shown in Figs. 6 and 8. Even with these improvements, the two Mie-based models are not as stable for gradient descent-based search as the HG model. Also notable is the inversely determined values of $\mu_d$ and $d$ at $\delta_{\min}$ being significantly different from the microscopically measured values, which may be due to the aggregation and settlement of the 11-$\mu$m spheres during signal measurement.

Finally, we have investigated the effect of uncertainty in measured signals on the RT parameters inversely determined by the HG sample mode. The values of the measured signals listed in Table I show that the relative errors of these signals average at about 2.7%. The RT parameters of the two sphere samples were determined by the inverse algorithm with the measured signals of $R_d$, $T_d$, and $T_f$ increased by 3.0% from their mean values in Table I. The percentage change varies from $-2.7\%$ to 3.0% for $\mu_s$ and from $-0.3\%$ to 0.3% for g from their values shown in Fig. 6 among the five wavelengths in the case of sample A. But the relative changes of $\mu_a$ are much larger, ranging from $-80\%$ to 0%, which indicates indeed a detection floor of $\mu_a$ around 0.2 mm$^{-1}$ for the proto-type system. In comparison, the relative changes of $\mu_s$ and g are similar in the case of sample B but those of $\mu_a$ decrease to a range of $-48\%$ to 0% since their values are between 0.27 and 0.42 mm$^{-1}$. It is clear from these results that the presented method of multiparameter spectrophotometry can yield accurate values of $\mu_s$ and g but has reduced sensitivity and accuracy for $\mu_a$ when its values are close to the detection floor and orders of magnitude smaller than those of $\mu_s$.

## V. Conclusion

We have developed a prototype system to test a new platform design for multiparameter spectrophotometric instruments for accurate characterization of homogeneous turbid samples by the RT theory. Two sphere suspension samples have been measured to determine inversely their RT parameters from 460 to 1000 nm and the system validation has been achieved by comparison to the RT parameters determined by the Mie theory for independent and single spheres. We focused on evaluation of the platform performance to solve inversely the RT parameters from the measured signals with three sample models. With an objective function $\delta$ and the criterion of $\delta \leq \delta_0$ for inverse solution, we have shown quantitatively that the HG sample model outperforms the two Mie-based sample models for all cases of the two samples at five wavelengths. These results demonstrate clearly that the HG function parameterized by g exhibits strong robustness in solving inverse light-scattering problems and extracting

RT parameters for spectroscopic analysis of turbid samples. By comparison, Mie-based phase functions and sample models are applicable only to problems in which light transport in a uniform suspension is dominated by scattering by independent and single spheres that are rarely the case for practical applications. Our results further demonstrate for the prototype system that the uncertainties in the measured signals and the inversely determined scattering parameters of $\mu_s$ and g can be kept to about 5% or less, while a detection floor of about 0.2 mm$^{-1}$ exists for $\mu_a$ in the cases of strongly turbid samples.

## References

[1] A. Lehmuskero, M. Skogen Chauton, and T. Boström, "Light and photosynthetic microalgae: A review of cellular-and molecular-scale optical processes," *Prog. Oceanogr.*, vol. 168, pp. 43–56, Nov. 2018.

[2] L. da Silva Dias, J. C. da Silva Junior, A. L. de Souza Maudeira Felicio, and J. A. de Franca, "A NIR photometer prototype with integrating sphere for the detection of added water in raw milk," *IEEE Trans. Instrum. Meas.*, vol. 67, no. 12, pp. 2812–2819, Dec. 2018.

[3] R. B. de Freitas, V. N. H. Silva, V. T. Maia, O. B. D. Santos, Y. M. de Arruda Calvette, and S. B. Fiaux, "Low-cost device to measure concentration of saccharomyces cerevisiae through methylene blue reduction," *IEEE Trans. Instrum. Meas.*, vol. 69, no. 5, pp. 2232–2238, May 2020.

[4] H. C. van de Hulst, *Multiple Light Scattering: Tables, Formulas and Applications*. New York, NY, USA: Academic, 1980.

[5] T. J. Farrell, M. S. Patterson, and B. Wilson, "A diffusion theory model of spatially resolved, steady-state diffuse reflectance for the noninvasive determination of tissue optical properties *in vivo*," *Med. Phys.*, vol. 19, no. 4, pp. 879–888, Jul. 1992.

[6] G. Bal, "Inverse transport theory and applications," *Inverse Problems*, vol. 25, no. 5, May 2009, Art. no. 053001.

[7] S. A. Prahl, M. J. C. van Gemert, and A. J. Welch, "Determining the optical properties of turbid media by using the adding–doubling method," *Appl. Opt.*, vol. 32, pp. 559–568, Feb. 1993.

[8] X. Ma, J. Q. Lu, and X. H. Hu, "Effect of surface roughness on determination of bulk tissue optical parameters," *Opt. Lett.*, vol. 28, pp. 2204–2206, Nov. 2003.

[9] C. Chen, J. Q. Lu, H. Ding, K. M. Jacobs, Y. Du, and X. H. Hu, "A primary method for determination of optical parameters of turbid samples and application to intralipid between 550 and 1630 nm," *Opt. Express*, vol. 14, pp. 7420–7435, Aug. 2006.

[10] B. Aernouts *et al.*, "Supercontinuum laser based optical characterization of Intralipid phantoms in the 500-2250 nm range," *Opt. Express*, vol. 21, pp. 32450–32467, Dec. 2013.

[11] H. J. Juttula, T. P. Kananen, and A. J. Makynen, "Instrument for measurement of optical parameters of turbid media by using diffuse reflectance of laser with oblique incidence angle," *IEEE Trans. Instrum. Meas.*, vol. 63, no. 5, pp. 1301–1309, May 2014.

[12] X. Liang *et al.*, "Spectrophotometric determination of turbid optical parameters without using an integrating sphere," *Appl. Opt.*, vol. 55, no. 8, pp. 2079–2085, Mar. 2016.

[13] P. Lemaillet *et al.*, "Correction of an adding-doubling inversion algorithm for the measurement of the optical parameters of turbid media," *Biomed. Opt. Express*, vol. 9, pp. 55–71, Jan. 2018.

[14] P. Tian, S. M. Mutisya, J. Jin, S. Zheng, J. Q. Lu, and X.-H. Hu, "Spectral determination of $\mu$a, $\mu$s and g from single and multiple scattering signals with one optically thick sample," *J. Quant. Spectrosc. Radiat. Transf.*, vol. 245, Apr. 2020, Art. no. 106868.

[15] S. L. Jacques, S. Roussel, and R. Samatham, "Polarized light imaging specifies the anisotropy of light scattering in the superficial layer of a tissue," *J. Biomed. Opt.*, vol. 21, no. 7, Jul. 2016, Art. no. 071115.

[16] M. P. Shepilov, "Asymmetry parameter for anomalous scattering of light in nanostructured glasses," *Opt. Lett.*, vol. 42, pp. 4513–4516, Nov. 2017.

[17] P. Tian, C. Chen, J. Jin, H. Hong, J. Q. Lu, and X. H. Hu, "Quantitative characterization of turbidity by radiative transfer based reflectance imaging," *Biomed. Opt. Express*, vol. 9, pp. 2081–2094, May 2018.

[18] T. J. Petzold, "Volume scattering functions for selected ocean waters," Scripps Inst. Oceanogr. (SIO), San Diego, CA, USA, Tech. Rep. AD-753 474, 1972.

[19] L. O. Reynolds and N. J. McCormick, "Approximate two-parameter phase function for light scattering," *J. Opt. Soc. Amer.*, vol. 70, no. 10, pp. 1206–1212, Oct. 1980.

[20] G. R. Fournier and J. L. Forand, "Analytic phase function for ocean water," *Proc. SPIE*, vol. 2258, Oct. 1994, pp. 194–201.

[21] S. Y. BenZvi, B. M. Connolly, J. A. J. Matthews, M. Prouza, E. F. Visbal, and S. Westerhoff, "Measurement of the aerosol phase function at the pierre auger observatory," *Astroparticle Phys.*, vol. 28, no. 3, pp. 312–320, Nov. 2007.

[22] W. Cong, H. Shen, A. Cong, Y. Wang, and G. Wang, "Modeling photon propagation in biological tissues using a generalized delta-eddington phase function," *Phys. Rev. E, Stat. Phys. Plasmas Fluids Relat. Interdiscip. Top.*, vol. 76, no. 5, Nov. 2007, Art. no. 051913.

[23] N. Tuchow, J. Broughton, and R. Kudela, "Sensitivity analysis of volume scattering phase functions," *Opt. Express*, vol. 24, pp. 18559–18570, Aug. 2016.

[24] L. C. Henyey and J. L. Greenstein, "Diffuse radiation in the galaxy," *Astrophys. J.*, vol. 93, pp. 70–83, Jan. 1941.

[25] A. N. Yaroslavsky, I. V. Yaroslavsky, T. Goldbach, and H.-J. Schwarzmaier, "Influence of the scattering phase function approximation on the optical properties of blood determined from the integrating sphere measurements," *J. Biomed. Opt.*, vol. 4, pp. 47–53, Jan. 1999.

[26] H. Ding *et al.*, "Angle-resolved mueller matrix study of light scattering by B-cells at three wavelengths of 442, 633, and 850 nm," *J. Biomed. Opt.*, vol. 12, no. 3, Feb. 2007, Art. no. 034032.

[27] H. Tan, R. Doerffer, T. Oishi, and A. Tanaka, "A new approach to measure the volume scattering function," *Opt. Express*, vol. 21, pp. 18697–18711, Aug. 2013.

[28] T. Harmel, M. Hieronymi, W. Slade, R. Röttgers, F. Roullier, and M. Chami, "Laboratory experiments for inter-comparison of three volume scattering meters to measure angular scattering properties of hydrosols," *Opt. Express*, vol. 24, no. 2, p. A234, Jan. 2016.

[29] J. R. Mourant, J. Boyer, A. H. Hielscher, and I. J. Bigio, "Influence of the scattering phase function on light transport measurements in turbid media performed with small source–detector separations," *Opt. Lett.*, vol. 21, no. 7, pp. 546–548, Apr. 1996.

[30] X. Ma, J. Q. Lu, R. S. Brock, K. M. Jacobs, P. Yang, and X.-H. Hu, "Determination of complex refractive index of polystyrene microspheres from 370 to 1610 nm," *Phys. Med. Biol.*, vol. 48, no. 24, pp. 4165–4172, Dec. 2003.

[31] Z. Song, K. Dong, X. H. Hu, and J. Q. Lu, "Monte Carlo simulation of converging laser beams propagating in biological materials," *Appl. Opt.*, vol. 38, pp. 2944–2949, May 1999.

[32] Y. Du, X. H. Hu, M. Cariveau, X. Ma, G. W. Kalmus, and J. Q. Lu, "Optical properties of porcine skin dermis between 900 nm and 1500 nm," *Phys. Med. Biol.*, vol. 46, no. 1, pp. 167–181, Jan. 2001.

[33] X. Chen *et al.*, "Fast method for inverse determination of optical parameters from two measured signals," *Opt. Lett.*, vol. 38, pp. 2095–2097, Dec. 2013.

[34] D. Toublanc, "Henyey–Greenstein and Mie phase functions in Monte Carlo radiative transfer computations," *Appl. Opt.*, vol. 35, no. 18, pp. 3270–3274, 1996.

[35] C. F. Bohren and D. R. Huffman, *Absorption and Scattering of Light by Small Particles*. New York, NY, USA: Wiley, 1983.

[36] G. Hale and M. Querry, "Optical constants of water in the 200 nm to 200 micrometer wavelength region," *Appl. Opt.*, vol. 12, pp. 555–563, Mar. 1973.

**Yonghong Qin** received the B.S. degree in electronic and information engineering from the Hunan Institute of Science and Technology, Yueyang, China, in 2018, where she is currently pursuing the M.S. degree in information and communication engineering.

Her current research interests are in the optical design and light scattering signal measurement with multiparameter spectrophotometry and parallel Monte Carlo simulations by GPU.

**Lin Zhao** received the M.S. degree in computer application technology from the Huazhong University of Science and Technology, Wuhan, China, in 2007, and the Ph.D. degree in control science and engineering from Central South University, Changsha, China, in 2017.

He is currently an Associate Professor with the Hunan Institute of Science and Technology, Yueyang, China, and conducts research in optical imaging, artificial intelligence, and computational modeling for optimal control of complex industrial processes.

**Stephen M. Mutisya** received the B.S. and M.S. degrees in physics from Virginia Commonwealth University, Richmond, VA, USA, in 2009 and 2011, respectively. He is currently a doctoral graduate student in the Department of Physics, East Carolina University, Greenville, NC, USA.

He also works as a Metrology Engineer with Intel Corporation, Albuquerque, NM, USA. His research specializes in the development of a new spectrophotometric method for turbidity characterization.

**Jiahong Jin** received the B.S. degree in applied mathematics and the M.S. degree in optics from Sun Yat-sen University, Guangzhou, China, in 2007 and 2014, respectively. He is currently pursuing the Ph.D. degree in biomedical physics with the Department of Physics, East Carolina University, Greenville, NC, USA.

He joined the Physics Faculty, Hunan Institute of Science and Technology, Yueyang, China, in 2014, and the Institute for Advanced Optics in 2016. He is conducting research in optical imaging of turbid materials and biological tissues and machine learning study on diffraction image data of cells.

**Peng Tian** received the B.S. degree from Hunan Normal University, Changsha, China, in 2000 and the M.S. and Ph.D. degrees in electronic science and technology from the Huazhong University of Science and Technology of China, Wuhan, China, in 2006 and 2011, respectively.

He is currently an Associate Professor with the Hunan Institute of Science and Technology, Yueyang, China, and has visited the Biomedical Laser Laboratory, Department of Physics, East Carolina University, Greenville, NC, USA, from 2016 to 2017, where he is currently a Visiting Faculty. His research interests are in the spectroscopic measurement and imaging of scattered light signals and efficient algorithm on solving inversion turbidity problems based on Monte Carlo simulations.

**Jun Q. Lu** received the B.S. and M.S. degrees from Nankai University, Tianjin, China, in 1983 and 1986, respectively, and the Ph.D. degree from the University of California at Irvine, Irvine, CA, USA, in 1991, all in physics.

She is currently with the Faculty of Physics, East Carolina University, Greenville, NC, USA. Her research areas include theoretical modeling, numerical simulations, and machine learning-based analysis of light scattering data acquired from biological cells and turbid samples.
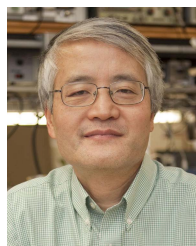
**Xin-Hua Hu** received the B.S. and M.S. degrees in physics from Nankai University, Tianjin, China, in 1982 and 1985, respectively, the M.S. degree in physics from Indiana University at Bloomington, Bloomington, IN, USA, and the Ph.D. degree in physics from the University of California at Irvine, Irvine, CA, USA, in 1991.

He joined the Physics Faculty, East Carolina University, Greenville, NC, USA, in 1995, and established the Biomedical Laser Laboratory. As a Professor, he conducts and directs research programs in optical imaging, theoretical modeling, and machine learning study of light scattering by human cells, in turbid materials and biological tissues. He is also interested in the development of novel instrumentation of spectrophotometry and flow cytometry based on spectral measurement and imaging of light scattering signals.